

# Amplification of three-dimensional perturbations during parallel vortex–cylinder interaction

X. LIU<sup>1</sup> AND J. S. MARSHALL<sup>2</sup>

<sup>1</sup>Department of Mechanical and Industrial Engineering, and IIHR – Hydrosience and Engineering,  
The University of Iowa, Iowa City, IA 52242, USA

<sup>2</sup>School of Engineering, The University of Vermont, Burlington, VT 05405, USA  
jeffm@cems.uvm.edu

(Received 28 March 2006 and in revised form 29 August 2006)

A computational study has been performed to examine the amplification of three-dimensional flow features as a vortex with small-amplitude helical perturbations impinges on a circular cylinder whose axis is parallel to the nominal vortex axis. For sufficiently weak vortices with sufficiently small core radius in an inviscid flow, three-dimensional perturbations on the vortex core are indefinitely amplified as the vortex wraps around the cylinder front surface. The paper focuses on the effect of viscosity in regulating amplification of three-dimensional disturbances and on assessing the ability of two-dimensional computations to accurately model parallel vortex–cylinder interaction problems. The computations are performed using a multi-block structured finite-volume method for an incompressible flow, with periodic boundary conditions along the cylinder axis. Growth of three-dimensional flow features is examined using a proper-orthogonal decomposition of the Fourier-transformed vorticity field in the azimuthal and axial directions. The interaction is examined for different axial wavelengths and amplitudes of the initial helical vortex waves and for three different Reynolds numbers.

---

## 1. Introduction

Impact of vortices shed from an upstream cylinder upon a downstream cylinder occurs in a variety of applications, including flow past bridge pilings, heat exchanger tubes, tall buildings, clusters of offshore platform risers, and parallel arrays of towed cables in a cross-flow behind a ship. The interaction of the wake of an upstream cylinder with a downstream cylinder has been examined by several investigators, using both two-dimensional numerical simulations (Li *et al.* 1991; Mittal, Kumar & Raghuvanshi 1997; Sun, Li & Roux 1993) and experiments (Brika & Laneville 1997; Kiya *et al.* 1980). A review of earlier work on the interaction between two cylinders is given by Zdravkovich (1977), and a review of vortex–body interaction in general, including the two-dimensional parallel vortex–cylinder interaction, is given by Rockwell (1998). These studies have shown that several different regimes of the wake flow of a cylinder pair occur depending on the ratio of cylinder spacing  $L$  to diameter  $d$ , as well as on the Reynolds number. When the spacing ratio is sufficiently small ( $L/d$  less than about 1.4), the pair of cylinders acts like a single bluff body and sheds only a single wake, whereas for larger values of spacing ratio the wake vortices shed by the upstream cylinder impinge on the face of the downstream cylinder. It is generally observed that the average drag coefficient of the downstream cylinder is much less than that of the upstream cylinder due to the reduction of mean velocity

within the upstream cylinder wake; however, the downstream cylinder exhibits greater fluctuation in drag coefficient due to the impinging vortices. Both the upstream and downstream cylinders exhibit an oscillating lift force, but the magnitude of the lift oscillations for the downstream cylinder is significantly greater than that for the upstream cylinder, again due to the effect of the impacting wake vortices.

The studies cited above concentrate on two-dimensional aspects of the cylinder wake interaction. Three-dimensional aspects of the interaction of a pair of yawed, parallel cylinders was investigated by Thakur, Liu & Marshall (2004), yielding experimental results obtained from laser-induced fluorescence flow visualization and from quantitative measurement of the wake velocity field with particle-image velocimetry, as well as three-dimensional computational results for a variety of cylinder yaw angles. For moderate yaw angles, the vortices shed from the upstream cylinder are nominally parallel to the cylinder axis sufficiently far from the cylinder leading edge, as was previously observed by Ramberg (1983). The wake vortices of the upstream cylinder advect back to impinge upon the downstream cylinder. The results of Thakur *et al.* (2004) indicate that the degree of three-dimensionality of the vortices increases as the vortices impinge upon the downstream cylinder, such that even though the wake of the upstream cylinder appears nominally two-dimensional, the flow becomes increasingly three-dimensional as the vortices shed from the upstream cylinder impinge upon the face of the downstream cylinder.

Amplification of three-dimensional perturbations as a vortex impinges on the front stagnation point of a downstream cylinder in the presence of a uniform flow is expected to occur for inviscid fluids owing to the presence of a cross-stream straining flow near the cylinder front stagnation point, which leads to a vortex instability resulting in growth of bending waves on the vortex core (Tsai & Widnall 1974; Moore & Saffman 1975). Because amplification of vortex perturbations occurs only as the vortex approaches very close to the cylinder surface, in real fluids the vortex flow field is expected to be significantly influenced by viscous interaction of the vortex with the cylinder boundary layer. The straining flow upstream of a cylinder is similarly found by Hunt (1973) and Britter, Hunt & Mumford (1979) to be responsible for amplification of the magnitude of the fluctuating azimuthal vorticity component as turbulence impinges on a cylinder. This type of vorticity amplification might occur as a limiting case of the near-parallel interaction problem considered in the present paper, should the vortex perturbations grow to such an extent that the vortex wraps around the front face of the cylinder.

The current study employs a proper-orthogonal decomposition (POD) method (Holmes, Lumley & Berkooz 1998) to quantify the amplification of three-dimensional perturbations as a vortex with small helical waves impinges on a cylinder, where the nominal axis of the unperturbed vortex is parallel to the cylinder axis. The study focuses on cases where the initial vortex perturbations are small, such that the vortex exhibits significant three-dimensional features only as it approaches close to the cylinder surface. The primary objective of the study is to examine the effects of viscous interaction and finite vortex core radius on regulating amplification of the three-dimensional vortex perturbations. A secondary objective is to determine the conditions under which the approximation of two-dimensional flow is reasonable for parallel vortex–cylinder interaction problems. These objectives are examined based on computations of vortex–cylinder interaction in a viscous incompressible fluid over a range of values of the helical vortex perturbation amplitude and wavelength and for three vortex Reynolds numbers, in order to characterize the observed amplification under different conditions.

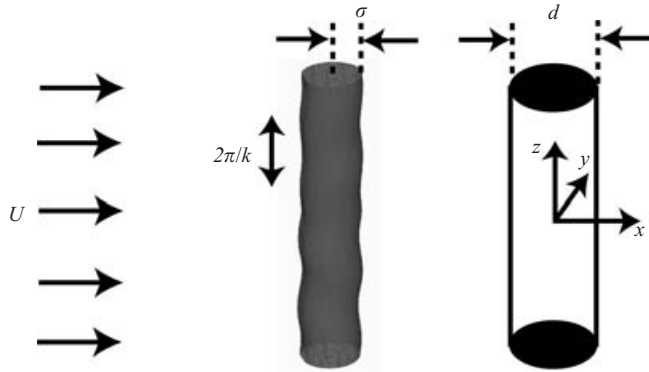


FIGURE 1. Schematic of the vortex prior to interaction with the cylinder, showing the Cartesian coordinate system and various parameters used in the computations.

In §2, we briefly describe the multi-block structured finite-volume method that is used for the viscous vortex–cylinder interaction problems, along with a grid-independence study. The POD method that is used to extract information on amplification of the three-dimensional vortex perturbations is described in §3, along with a further grid-independence study. The effect of viscosity on the three-dimensional perturbation amplification is examined for cases with a range of initial helical wave amplitudes and wavenumbers in §4 for a Reynolds number of 300. The effect of higher Reynolds numbers on amplification of the three-dimensional vortex perturbations is examined in §5. The issue of mode selection during vortex wave amplification is examined for a problem where the initial vortex has perturbations with a range of different wavenumbers in §6. Conclusions are given in §7.

## 2. Computational method

Computations of three-dimensional vortex–cylinder interaction are performed using a finite-volume method with a block-structured grid (Lai 2000). The flow is assumed to be incompressible with uniform density and viscosity. The control volumes (cells) have a quadrilateral cross-section in the  $x$ ,  $y$  (cross-stream) plane and uniform spacing in the axial ( $z$ ) direction. The numerical method stores all dependent variables at the cell centres and uses a novel interpolation method to yield a second-order-accurate approximation of the diffusive and convective fluxes on the cell boundaries for arbitrary meshes. The PISO algorithm (Issa 1985) is used to couple momentum and continuity equations. In order to provide additional numerical stability, the time derivative is weighted between a second-order time derivative approximation and a first-order upwind approximation, with characteristically about 90 : 10 weighting ratio.

A schematic of the vortex–cylinder interaction is given in figure 1, showing the orientation of the Cartesian coordinate system used in the flow computations and the orientation of the uniform flow velocity  $U$ , the nominal vortex core radius  $\sigma$ , the cylinder diameter  $d$ , and the vortex perturbation wavelength  $2\pi/k_h$ . Vortex impact on a cylinder is influenced by a wide range of dimensionless parameters, including Reynolds number  $Re = Ud/\nu$ , circulation parameter  $G = \Gamma/U\sigma$ , dimensionless vortex core radius  $R = \sigma/d$ , and helical perturbation wavenumber  $K = k_h d$  and amplitude  $A = a/d$ . All variables in the paper are non-dimensionalized using  $d$  and  $d/U$  as length and time scales, respectively. A listing of the different computations performed is given in table 1.

---

Case	$Re = Ud/\nu$	$A = a/d$	$K = k_n d$
1	300	0	
2	300	0.01	4
3	300	0.03	4
4	300	0.06	4
5	300	0.2	4
6	300	0.03	2
7	300	0.03	8
8	600	0.06	4
9	1200	0.06	4
10	300	0.06	1–10

---

TABLE 1. Summary of different computational cases examined, with  $G = \Gamma/U\sigma = 10$  and  $R = \sigma/d = 0.5$  for all cases.

A multi-block structured grid is employed to discretize the flow in the cross-stream  $(x, y)$  plane, which extends from  $x = -7.14$  to  $x = 12.38$  in the streamwise direction and from  $y = -3.57$  to  $y = 3.57$  in the transverse direction. The cylinder axis coincides with the  $z$ -axis. The grid is very fine near the cylinder and just upstream of the cylinder in order to resolve the incident vortex interaction with the cylinder face. The boundary conditions consist of inlet and outlet conditions on the left- and right-hand grid boundaries, the symmetry condition on the top and bottom grid boundaries, and periodic boundary conditions along the cylinder axis. In order to induce onset of vortex shedding from the cylinder, the inlet velocity has a small perturbation in the  $x, y$  plane, given by

$$u_{inlet}(y) = 1 + 0.05 \sin[2\pi(y - y_B)/(y_T - y_B)], \quad (1)$$

where  $y_T$  and  $y_B$  denote the positions of the top and bottom boundaries, respectively. The time step in all computations is held fixed at  $\Delta t = 0.02$ .

Independence of the computational results to choice of cross-sectional grid is examined by comparing a two-dimensional computation (in the  $x, y$  plane) for flow past a cylinder at  $Re = 300$ , with both a fine mesh (Mesh 1; 19 716 grid points) and a coarser mesh (Mesh 2; 10 682 grid points). A plot of the drag and lift coefficients for the two grids is given in figure 2, which indicates close agreement between the computations with the two grids. Experimental data reported by Fleischman & Sallet (1981) for  $Re = 300$  gives the mean drag coefficient as  $\bar{C}_d = 1.4 \pm 0.1$ , the amplitude of variation of the lift coefficient as  $C_{\ell,amp} = 0.6 \pm 0.25$ , and the Strouhal number as  $St = 0.21 \pm 0.01$ , yielding an oscillation period of  $T = 1/St = 4.76$ . These values are in reasonably good agreement with the computational results. Three-dimensional computations are performed by extended the fine mesh (Mesh 1) in the  $x, y$  plane using 100 uniform increments in the axial ( $z$ ) direction from  $z = -\pi$  to  $z = \pi$ . Grid independence in the  $z$ -direction is examined further in §3.

The computations are initialized using a three-step process. In the first step, we compute steady uniform flow past the cylinder with no vortex present. In the second step, we compute unsteady flow past the cylinder, allowing the Kármán vortex street to fully develop. In the third step, we use a triply periodic Fourier spectral code to compute the velocity field induced by a helical vortex with a specified dimensionless perturbation amplitude  $A$  and wavenumber  $K$ , and nominal axis located at  $(x, y) = (-2.57, 0)$ . A rectangular Cartesian grid is used for the helical vortex computation with the same exterior dimensions as the grid used for the vortex–cylinder interaction

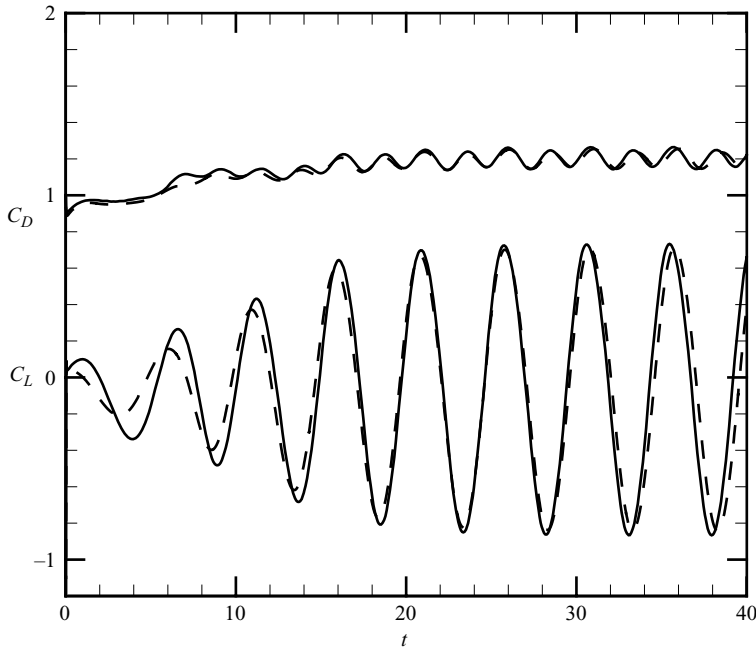


FIGURE 2. Variation of lift and drag coefficients with time for two-dimensional flow past a cylinder with Mesh 2 (dashed line) and Mesh 1 (solid line).

problem. The velocity field from the helical vortex computation is then interpolated onto the block-structured grid and added to the velocity obtained from the computation of unsteady uniform flow past a cylinder to obtain the initial condition for the vortex–cylinder interaction computation. While this initial condition does not exactly satisfy the no-slip condition on the cylinder surface, which results in production of a weak vortex sheet on the cylinder at the initial time, the vorticity associated with this vortex sheet is small and passes downstream before the vortex interacts significantly with the cylinder. Of somewhat greater concern is the weak vortex sheet generated at the inlet boundary due to the vortex-induced velocity in the initial condition. This vortex sheet is advected into the vortex over time by the upstream uniform flow. The strength of this upstream vortex sheet can be held at a small level by extending the grid a sufficient distance upstream of the vortex, so as to increase the distance between the vortex and the inlet boundary. In the computations presented in the paper, the vorticity in the upstream vortex sheet is less than 1% of the nominal vorticity magnitude within the initial helical vortex. Cases with different upstream inlet boundary locations have been examined to verify that the upstream vortex sheet has negligible effect on the reported computational results.

### 3. Proper orthogonal decomposition

Proper-orthogonal decomposition (POD) provides a method for extracting the contribution of different axial and azimuthal wavenumbers of the velocity and vorticity fields characterizing a three-dimensional flow field on a cylindrical polar grid. We initiate the POD analysis by interpolating the vorticity field into a cylindrical polar grid, which covers a portion of the full block-structured grid extending out to a radius  $R = 3.57$  from the cylinder axis.

The POD acts to project a field under examination, say  $u(\mathbf{x}, t)$ , onto a set of orthogonal eigenfunctions  $\{\phi^{(n)}\}$  that are fitted to the given field, such that most of the ‘energy’ of the field is contained in the first few terms (and often the first term) of this expansion. We employ a simplified ‘slice POD’ procedure, related to that of Gamard *et al.* (2002), which employs fixed-time, Fourier-transformed velocity and vorticity fields in the axial and azimuthal directions to yield

$$2\pi \int_0^\infty R(t, r, r'; m, k) \phi^{(n)}(t, r'; m, k) r' dr' = \lambda^{(n)} \phi^{(n)}(t, r; m, k), \quad (2)$$

where  $\lambda^{(n)}$  is the  $n$ th POD eigenvalue,  $R(t, r, r'; m, k) = \hat{u}(t, r; m, k) \hat{u}(t, r'; m, k)$  is the radial correlation of the azimuthal and axial Fourier transforms of the scalar function  $u(t, r, \theta, x)$ , and  $m$  and  $k$  are the azimuthal and axial wavenumbers, respectively. From the Hilbert–Schmidt theorem, the scalar  $\hat{u}$  can be decomposed as a sum over the eigenfunctions as

$$\hat{u}(t, r; m, k) = \sum_{n=1}^{\infty} a_n(t; m, k) \phi^{(n)}(t, r; m, k), \quad (3)$$

where  $a_n$  are the expansion coefficients. It is convenient for numerical solution of (2) to make the kernel symmetric by defining new eigenfunctions  $\psi^{(n)} \equiv r^{1/2} \phi^{(n)}$  to give

$$2\pi \int_0^\infty [r^{1/2} R(t, r, r'; m, k) (r')^{1/2}] \psi^{(n)}(t, r'; m, k) dr' = \lambda^{(n)} \psi^{(n)}(t, r; m, k). \quad (4)$$

The calculations indicate that nearly all of the signal energy is contained in the first eigenmode. The POD method provides a means to compare the energy contained in different azimuthal and axial modes of the flow by comparing the first eigenvalue for the corresponding  $m$  and  $k$  values. In performing the POD analysis, the vorticity field is first interpolated onto the cylindrical polar grid using a linear Lagrange interpolation. The POD eigenvalues are computed by taking the discrete Fourier transform in the azimuthal and axial directions, discretizing the integral over  $r$  in (4), and solving for the first few eigenvalues of the resulting algebraic eigenvalue problem for each  $m$  and  $k$  value using the DSYEVX subroutine in the LAPACK package.

The first POD eigenvalue  $\lambda_i$  is obtained as a function of the azimuthal and axial wavenumbers,  $m$  and  $k$ , for all vorticity components. Summing the POD eigenvalues over all azimuthal wavenumbers yields a measure  $\bar{\lambda}_i(k)$  of the  $i$ th vorticity component as a function of the axial wavenumber  $k$ . For a purely two-dimensional flow, the enstrophy would be clustered at the  $k=0$  wavenumber, such that the value of POD eigenvalues for  $k > 0$  modes provides an indication of the magnitude of different three-dimensional disturbances of the vorticity field. The helical vortex perturbations are initiated with a specific dimensionless axial wavenumber  $K$ , which is varied in the different computations. By observing the time variation of  $\bar{\lambda}_i(k)$  for different wavenumber values and for cases with different helical perturbation wavenumbers and amplitudes, we can determine how the incident vortex perturbations amplify and how they interact with the ambient cylinder wake streamwise vortices.

The POD analysis approach is used to examine the sensitivity of the flow to the axial grid resolution for a case with helical perturbation amplitude  $A=0.06$  and wavenumber  $K=4$  and Reynolds number  $Re=300$  (Case 4) by comparing computations for helical vortex impingement on the cylinder for a fine grid with 100 points in the axial direction (Mesh 1) with results for a coarser grid with 50 points in the axial direction (Mesh 3). The first POD eigenvalue of the radial vorticity

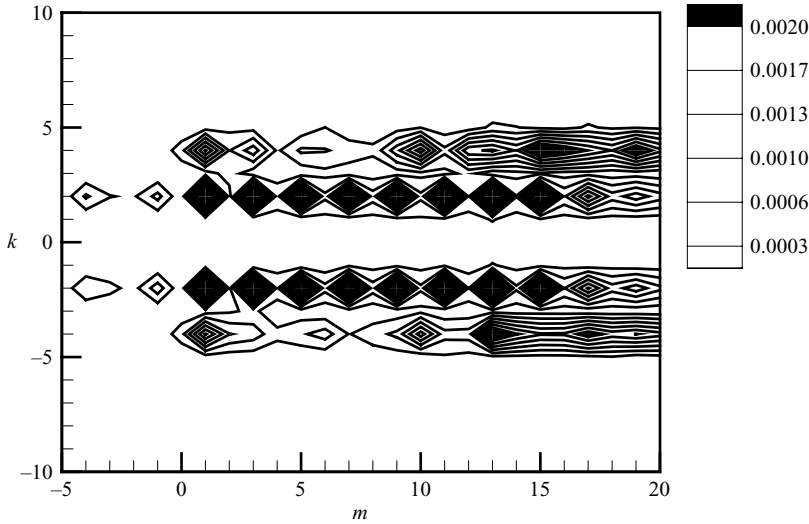


FIGURE 3. First POD eigenvalue of the radial vorticity component for Case 4 at  $t = 3$ , plotted as a function of the azimuthal and axial wavenumbers.

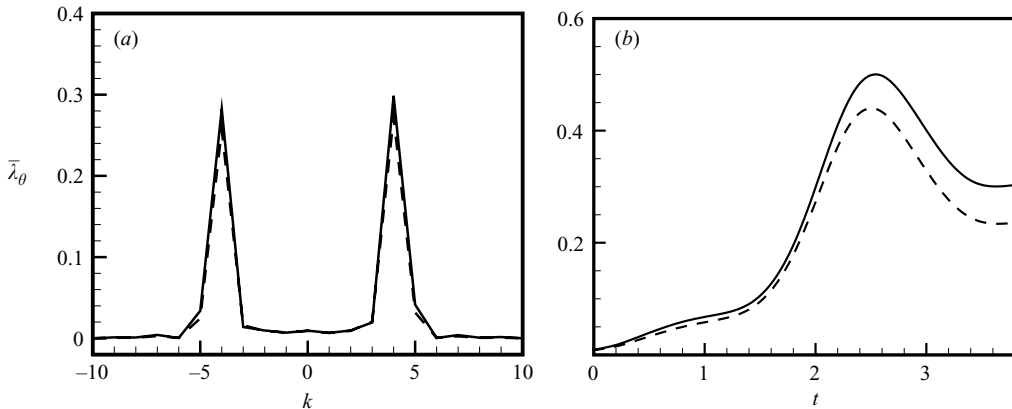


FIGURE 4. POD eigenvalues of the azimuthal vorticity summed in the azimuthal direction ( $\bar{\lambda}_\theta$ ) showing amplification of three-dimensional disturbances, for Case 4 with Mesh 3 (dashed line) and Mesh 1 (solid line), showing (a) variation of  $\bar{\lambda}_\theta$  with axial wavenumber at time  $t = 2$  and (b) variation of  $\bar{\lambda}_\theta$  with time for  $k = 4$ .

component ( $\lambda_r$ ) for all axial and azimuthal wavenumbers,  $k$  and  $m$ , is shown in the contour plot in figure 3 for the fine mesh (Mesh 1) at time  $t = 3$ . The POD eigenvalues are dominated by axial wavenumbers in the interval  $1 \leq k \leq 6$ , whereas the vorticity field exhibits broad spectral variation in the azimuthal wavenumber. The POD eigenvalues are summed over all values of the azimuthal wavenumber to compute the measures  $\bar{\lambda}_r$ ,  $\bar{\lambda}_\theta$  and  $\bar{\lambda}_z$ , which are used to determine how the enstrophy associated with each vorticity component varies with axial wavenumber. In figure 4(a), we plot  $\bar{\lambda}_\theta$  as a function of the axial wavenumber at time  $t = 2$  for both the coarse and fine meshes. The time variation of the POD eigenvalue with  $k = 4$  (corresponding to the wavenumber of the initial helical perturbation) is shown in figure 4(b). The dramatic growth of the azimuthal vorticity POD eigenvalue corresponding to the  $k = 4$

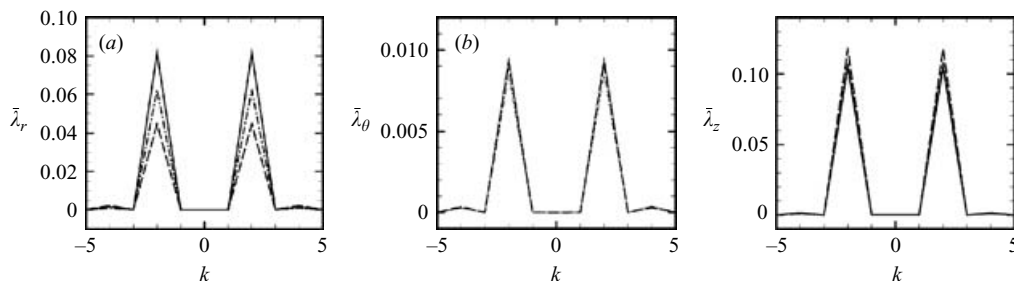


FIGURE 5. POD eigenvalues of the radial, azimuthal and axial vorticity components for impact of a straight vortex on a circular cylinder (Case 1) at time  $t=1$  (dashed line),  $t=2$  (dashed-dotted line), and  $t=3$  (solid line), as a function of axial wavenumber.

axial wavenumber as the vortex approaches the cylinder is indicative of amplification of the three-dimensional vortex perturbations. The POD eigenvalues for the coarse and fine grids are nearly identical at  $t=2$  for all axial wavenumbers (figure 4a). Near the end of the vortex–cylinder impact, small differences appear in the POD results obtained by the two grids for the higher wavenumber modes, as shown in figure 4(b) for  $t > 2.4$ , leading to a difference in predicted peak POD value of about 15 % by the end of the computation for the  $k=4$  mode. The qualitative trends for the results predicted with the coarse and fine grids are the same in all cases. All further computations in the paper are performed using the fine mesh (Mesh 1).

#### 4. Three-dimensional wave amplification – effects of perturbation amplitude and wavenumber

The cylinder wake with no upstream vortex exhibits two types of streamwise vortices (Mode A and Mode B) each with a specific axial wavenumber band, as indicated in the stability analysis of Barkley & Henderson (1996). For Reynolds numbers  $Re$  slightly greater than about 190, the cylinder wake exhibits streamwise vortices which are dominated by Mode A structures, corresponding to axial wavenumber in the interval  $1.5 \leq k \leq 2.1$ . As the Reynolds number increases above about 230, the Mode B structures begin to develop having wavenumbers in the interval  $5 \leq k \leq 8$ , with a broad Reynolds number interval where both types of structures co-exist (Williamson 1996).

It is useful to first examine a case where the incident vortex is perfectly columnar, with no three-dimensional perturbations. POD eigenvalues  $\bar{\lambda}_i$  of the radial, azimuthal and axial vorticity components for impact of a columnar vortex on a circular cylinder (Case 1) are plotted in figure 5 at times  $t=1, 2$  and  $3$  as a function of axial wavenumber. These times correspond to conditions where the vortex is located about two cylinder diameters upstream of the cylinder ( $t=1$ ), about one cylinder diameter upstream ( $t=2$ ), and impinging directly on the cylinder ( $t=3$ ). For the axial POD eigenvalue, we have subtracted the large  $k=0$  mode so as to more clearly view the other modes. The POD eigenvalues for all three vorticity components are dominated by the  $k=2$  mode, corresponding to the Mode A cylinder wake vortices. As the vortex approaches the cylinder and impinges upon the cylinder face, the peak POD eigenvalue of the radial vorticity increases to about 175 % of its initial value, corresponding to substantial increase in strength of the wake vortices. The POD eigenvalue of the azimuthal and axial vorticity components, on the other hand, remain nearly constant



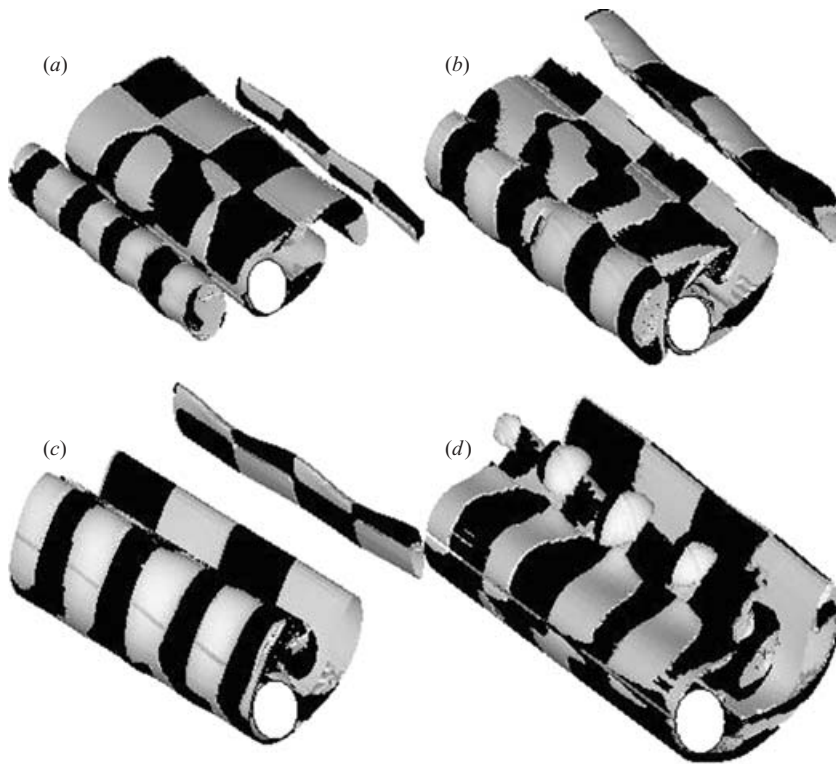


FIGURE 6. Iso-surface of vorticity magnitude ( $\omega=2$ ) in the near-wake for vortex–cylinder impact (Case 4) at times (a)  $t=1$ , (b) 2, (c) 3, and (d) 4. The surface is shaded grey in regions with positive streamwise vorticity component and black in regions with negative streamwise vorticity component.

as the vortex approaches the cylinder. Also, the values of the azimuthal vorticity POD eigenvalue are nearly an order of magnitude smaller than those of the radial and axial vorticity POD eigenvalues. The  $k=0$  mode of the axial vorticity POD eigenvalue increases by about 125% as the vortex approaches, corresponding to an increased velocity on the lower side of the cylinder resulting in a greater maximum vorticity value in the cylinder boundary layer.

The development of vortex wave amplification is examined in detail for Case 4, with initial wave amplitude  $A=0.06$  and axial wavenumber  $K=4$ . An iso-surface of vorticity magnitude ( $\omega=2.0$ ) is plotted in figure 6 at times  $t=1, 2, 3$  and 4, showing the initial helical waves on the vortex core and the development of the waves as the vortex impinges upon the cylinder and passes into the cylinder wake. The iso-surface is shaded grey for regions with positive streamwise vorticity and black for regions with negative streamwise vorticity. Streamwise vorticity ( $\omega_x$ ) contours in the cross-sectional plane  $x=1.4$ , which cuts across the cylinder wake just downstream of the cylinder, are plotted in figure 7 at the same four times as in figure 6. For the first three times, the vorticity contours in the cross-sectional plane in figure 7 are dominated by the  $k=2$  streamwise wake vortices. These streamwise vortices move up and down in the wake, and change the sign of the streamwise vorticity, corresponding to the natural shedding cycle of the Kármán wake vortices. In the last frame (figure 7d), the vorticity from the impinging vortex has advected back into the cylinder wake. In this frame,

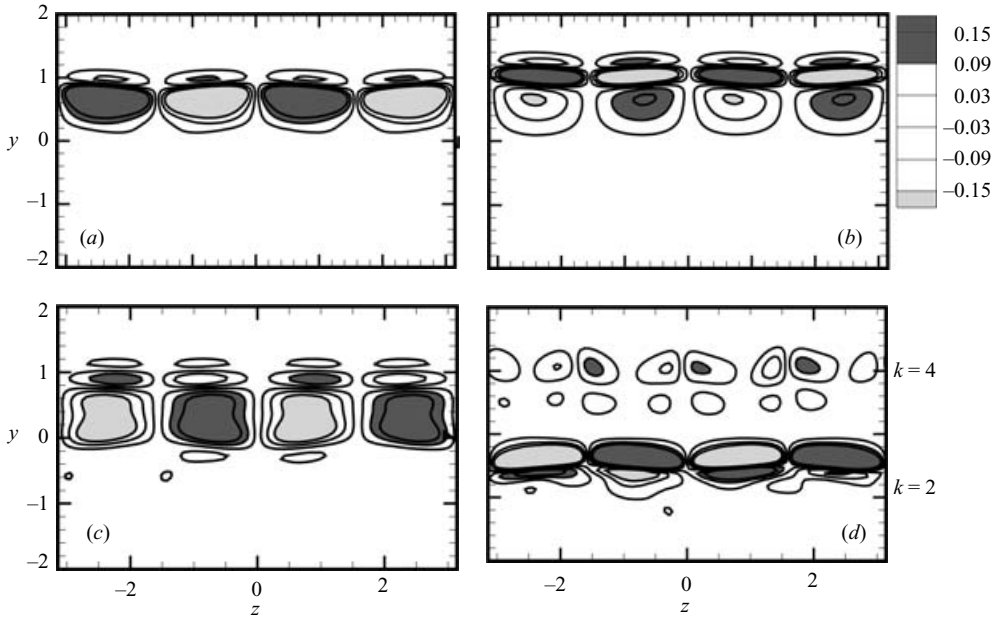


FIGURE 7. Streamwise vorticity ( $\omega_x$ ) contours at the cross-sectional plane  $x = 1.4$  for Case 4 at times (a)  $t = 1$ , (b) 2, (c) 3, and (d) 4. The final frame exhibits both wavenumber  $k = 2$  and wavenumber  $k = 4$  vorticity patterns.

we observe a row of the  $k = 2$  Mode A wake vortices along the bottom and a row of the  $k = 4$  perturbations from the impinging vortex along the top. These results, as well as the POD results to follow, indicate that the cylinder wake vortices and the three-dimensional perturbations of the impinging vortex maintain their individual wavenumbers and do not significantly interact, at least for cases with relatively small initial vortex wave amplitude.

#### *Effect of initial perturbation amplitude*

Amplification of three-dimensional vortex perturbations is best examined using the POD eigenvalues for the different vorticity components, since in this way we can extract a measure of the enstrophy associated with each axial wavenumber mode. Cases are examined for values of the initial vortex wave amplitude of  $A = 0.01, 0.03, 0.06$  and  $0.2$ , with all other parameters held to the same values (Cases 2–5). In figure 8, we plot the POD eigenvalues  $\bar{\lambda}_i$ , summed over all azimuthal modes, as a function of axial wavenumber for each vorticity component at times  $t = 1, 2$ , and  $3$  for cases with initial wave amplitude  $A = 0.01, 0.03$ , and  $0.06$ . The corresponding time variation of the  $k = 4$  mode, corresponding to the initial vortex perturbation wavenumber, is plotted in figure 9. We have again subtracted the axisymmetric  $k = 0$  mode from the axial vorticity component POD eigenvalues plots in figures 8 and 9 in order to focus on the influence of the three-dimensional vortex perturbations.

The radial vorticity eigenvalue exhibits peaks in figure 8 at  $k = 2$  and  $4$ , but also has non-negligible contributions from wavenumbers from the  $k = 3, 5$  and  $8$  modes, where the last mode increases substantially as the vortex impacts on the cylinder. All three cases, with three different initial vortex wave amplitudes, exhibit nearly the same POD eigenvalues for the  $k = 2$  mode, corresponding to the ambient Mode A wake vortices. This observation is further evidence that the three-dimensional vortex

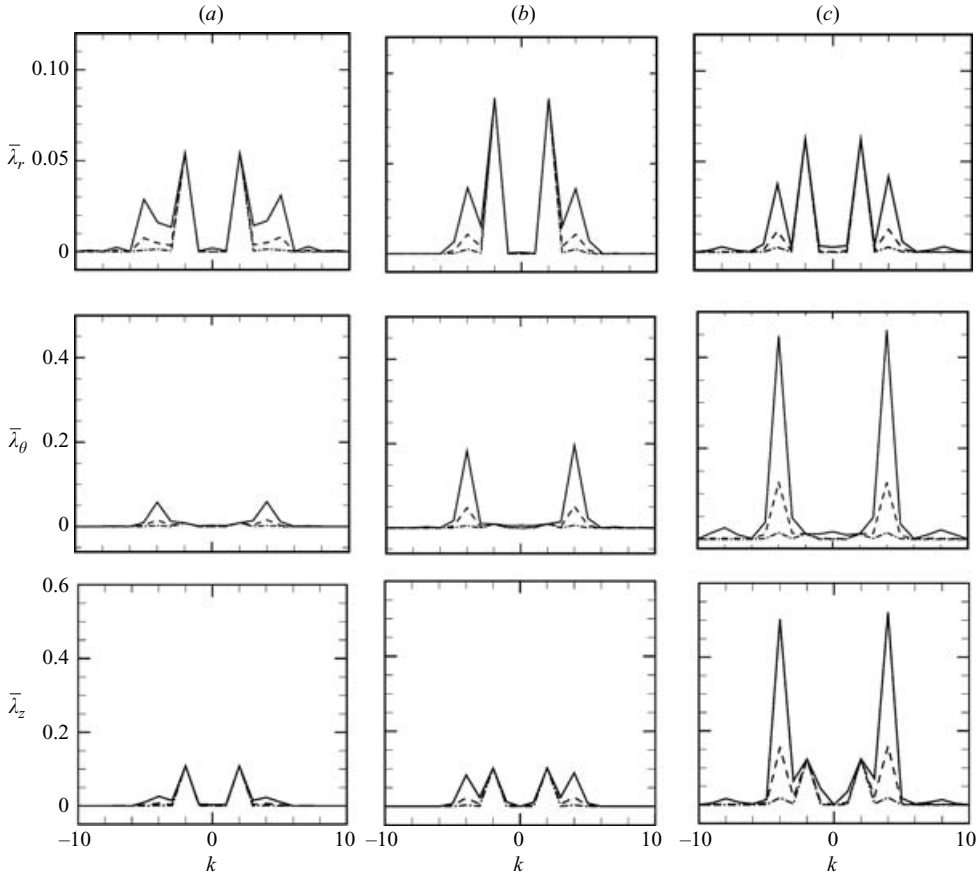


FIGURE 8. POD eigenvalues (summed over the azimuthal wavenumbers) for the radial, azimuthal and axial vorticity components at times (a)  $t = 1$ , (b)  $t = 2$ , and (c)  $t = 3$  for cases with initial helical wave amplitudes  $A = 0.06$  (Case 4, solid line),  $A = 0.03$  (Case 3, dashed line), and  $A = 0.01$  (Case 2, dashed-dotted line).

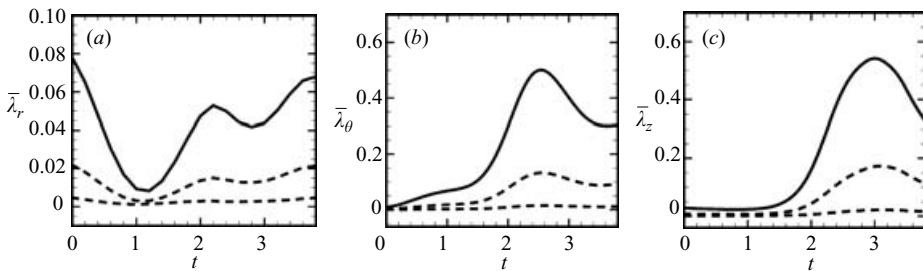


FIGURE 9. Time variation of POD eigenvalues for the (a) radial, (b) azimuthal and (c) axial vorticity components (summed over the azimuthal wavenumbers) for axial wavenumber  $k = 4$ , with initial helical wave amplitude  $A = 0.06$  (Case 4, solid line),  $A = 0.03$  (Case 3, dashed line), and  $A = 0.01$  (Case 2, dashed-dotted line).

perturbations have little effect on the cylinder streamwise wake vortices. The  $k = 4$  mode of the radial vorticity component exhibits an initial decrease between times  $0 \leq t \leq 1$  as the vortex approaches the cylinder, which is associated with the fact that

Case	$\bar{\lambda}_{z,H}$	$\bar{\lambda}_{z,S}$	$\bar{\lambda}_{z,I}$	$\frac{\bar{\lambda}_{z,H}}{\bar{\lambda}_{z,I}}$	$\frac{\bar{\lambda}_{z,H}}{\bar{\lambda}_{z,S}}$
2	0.0216	0.00124	0.000818	26.4	17.4
3	0.172	0.00124	0.00717	24.0	139
4	0.542	0.00124	0.0280	19.3	437
5	1.77	0.00124	0.247	7.17	1430
6	0.156	0.126	0.00758	20.6	1.24
7	0.0757	$6.36 \times 10^{-7}$	0.00560	13.5	$1.19 \times 10^5$
8	1.33	0.502	0.0285	46.7	2.65
9	1.88	0.579	0.0284	66.2	3.25

TABLE 2. Amplification measures for three-dimensional flow Cases 2–9.

the vortex perturbations are becoming increasingly aligned in the azimuthal direction during this stage of the interaction. Comparison of figures 8(b) and 8(c) indicates substantial growth of the  $k = 4$  mode radial vorticity eigenvalue as the vortex impacts on the cylinder face in the interval  $2 \leq t \leq 3$ .

The  $k = 4$  modes of both the axial and azimuthal vorticity eigenvalues exhibit very significant amplification during the vortex impact on the cylinder face. For both vorticity components, the POD eigenvalues peak at about  $t = 3$ , as the vortex nominal position coincides with the cylinder centre, and then decrease as the vortex passes into the cylinder wake. As was similarly noted for the radial vorticity eigenvalues, the higher wavenumber  $k = 8$  mode exhibits substantial increase in the azimuthal and axial vorticity fields as the vortex impinges on the cylinder face (near  $t = 3$ ), but the magnitude of the  $k = 8$  mode is always much smaller than the primary  $k = 4$  mode.

Amplification of the vortex three-dimensional perturbations is quantified based on ratios of three measures of the perturbation ‘size’: (i) the peak value of  $\bar{\lambda}_z$  as the perturbed vortex approaches the cylinder ( $\bar{\lambda}_{z,H}$ ), (ii) the value of  $\bar{\lambda}_z$  for the initial helical vortex with no cylinder wake present ( $\bar{\lambda}_{z,I}$ ), and (iii) the peak value of  $\bar{\lambda}_z$  for an initially straight vortex approaching the cylinder ( $\bar{\lambda}_{z,S}$ ). All of these measures are computed for axial wavenumber  $k = K$ , corresponding to the initial wavenumber of the helical perturbation. The values of these measures are listed in table 2 for the different three-dimensional computations reported in the paper. The ratio  $\bar{\lambda}_{z,H}/\bar{\lambda}_{z,S}$  provides a measure of the relative contributions of the impinging vortex and the cylinder wake on the POD eigenvalues. When  $\bar{\lambda}_{z,H}/\bar{\lambda}_{z,S} \gg 1$ , the peak POD eigenvalue is dominated by amplification of the three-dimensional perturbations of the impinging vortex. In this case, the ratio  $\bar{\lambda}_{z,H}/\bar{\lambda}_{z,I}$  provides a measure of the amplification of the three-dimensional perturbations due to impingement of the vortex upon the cylinder.

For the different initial vortex wave amplitudes considered in Cases 2–5, the value of the ratio  $\bar{\lambda}_{z,H}/\bar{\lambda}_{z,S}$  increases steadily from 17 to 1430 as the initial wave amplitude increases. In all of these cases, the amplification measure  $\bar{\lambda}_{z,H}$  is dominated by the helical vortex perturbations, and the cylinder wake exhibits very small eigenvalues at this wavenumber. For the three cases with smallest initial amplitude ( $A = 0.01, 0.03$ , and  $0.06$ ), the amplification ratio  $\bar{\lambda}_{z,H}/\bar{\lambda}_{z,I}$  is 26.4, 24.0, and 19.3, respectively. The fact that these ratios differ by only about 30% while  $\bar{\lambda}_{z,I}$  and  $\bar{\lambda}_{z,H}$  individually change by over a factor of 30 suggests that the amplification factor becomes independent of perturbation amplitude for sufficiently small values of the initial amplitude. For the case with  $A = 0.2$ , nonlinear effects appear to play a much greater role in regulating the amplification, and the amplification ratio  $\bar{\lambda}_{z,H}/\bar{\lambda}_{z,I}$  drops significantly to 7.2.

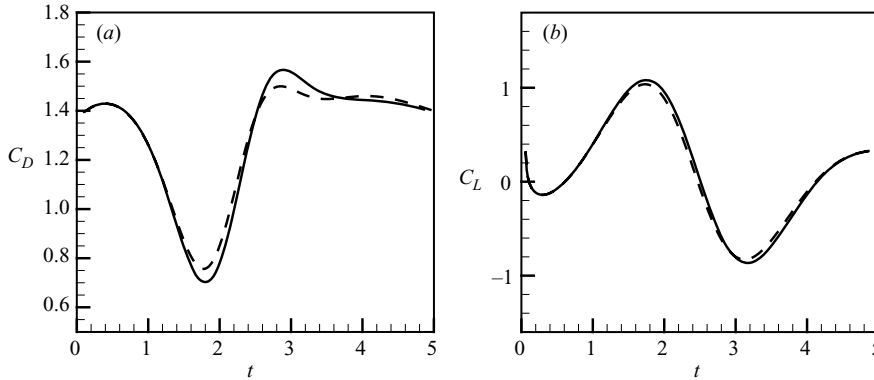


FIGURE 10. Time variation of drag and lift coefficients for cases with initial helical wave amplitude  $A=0.2$  (Case 5, solid line) and the straight vortex (Case 1, dashed line).

The drag and lift coefficients for Cases 2–4, with initial helical wave amplitudes of  $A=0.01$ ,  $0.03$ , and  $0.06$ , are nearly identical to those for the straight vortex (Case 1). The drag and lift coefficients for Case 5, with initial vortex wave amplitude  $A=0.2$ , are compared with those for the straight vortex case in figure 10. Even for initial wave amplitudes as high as 20% of the vortex core radius, the drag force is found to differ from that for a straight vortex by at most 7%, and the difference in lift coefficient is even smaller. This close agreement indicates that even though three-dimensional perturbations exhibit significant amplification as a vortex impinges on the cylinder face, the three-dimensional perturbations do not have a significant influence on the cylinder force, at least for cases with relatively small-amplitude vortex waves as considered in the present paper.

#### *Effect of initial perturbation wavenumber*

The effect of initial perturbation wavenumber is examined by comparison of the time variation of the POD eigenvalues  $\bar{\lambda}_i$  of the three vorticity components for the  $k=2$ , 4 and 8 modes in figure 11 for cases with initial helix wavenumber  $K=2$ , 4 and 8 (Cases 6, 3 and 7). For each of these cases, we observe a significant effect of the three-dimensional perturbations only for the mode where the axial wavenumber  $k$  is equal to the initial wavenumber  $K$  of the helical vortex waves.

For  $K=2$  (Case 6), the initial helical vortex waves have the same axial wavenumber as the streamwise Mode A wake vortices. For the  $k=2$  mode, we observe only a slight difference in the radial vorticity eigenvalue due to the three-dimensional perturbations, indicating that the radial vorticity eigenvalue is primarily dominated by the streamwise wake vortices. The azimuthal and axial vorticity eigenvalues exhibit significant amplification for the  $K=2$  perturbations, but the amount of amplification is significantly less than that for higher perturbation wavenumbers. Both the  $K=4$  and  $K=8$  cases exhibit a similar degree of amplification of the azimuthal vorticity eigenvalues. However, the amplification of the axial vorticity eigenvalues for the  $K=8$  case is less than half that for the  $K=4$  case.

The amplification measures for Cases 3, 6 and 7 listed in table 2 indicate that for Case 6 (with  $K=2$ ), the amplification measure  $\bar{\lambda}_{z,H}$  is significantly influenced by the Mode A streamwise vortices in the cylinder wake, with the corresponding ratio  $\bar{\lambda}_{z,H}/\bar{\lambda}_{z,S}=1.24$ . For this case, the ratio  $\bar{\lambda}_{z,H}/\bar{\lambda}_{z,I}$  is therefore not indicative of amplification of the impinging vortex perturbations. On the other hand, for Case 7

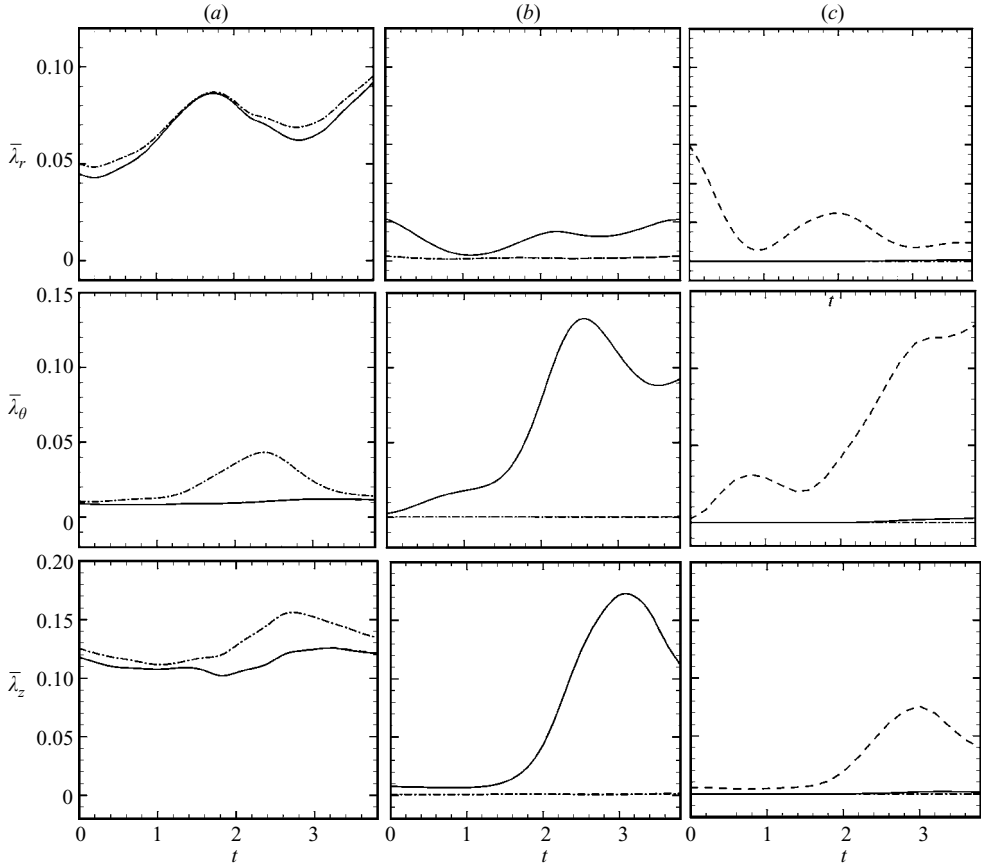


FIGURE 11. Time variation of POD eigenvalues (summed over the azimuthal wavenumbers) for the radial, azimuthal and axial vorticity components for cases with initial helical wavenumbers  $K = 2$  (Case 6, dashed-dotted line),  $K = 4$  (Case 3, solid line), and  $K = 8$  (Case 7, dashed line). The eigenvalues are plotted for axial wavenumbers (a)  $k = 2$ , (b)  $k = 4$  and (c)  $k = 8$ .

(with  $K = 8$ ) the ratio  $\bar{\lambda}_{z,H}/\bar{\lambda}_{z,S} = O(10^5)$ , so the cylinder wake has little effect for this wavenumber. The corresponding amplification ratios for the  $K = 4$  and  $K = 8$  cases are  $\bar{\lambda}_{z,H}/\bar{\lambda}_{z,I} = 24.0$  and  $13.5$ , respectively, indicating slightly greater amplification of the impinging vortex perturbations for the  $K = 4$  case. Further analysis of amplification at different perturbation wavenumbers is given in §6, in which we examine a case in which the vortex is initiated with a broad spectrum of initial wavenumbers.

### 5. Three-dimensional wave amplification – effects of Reynolds number

The effect of Reynolds number was examined by repeating the computation with perturbation wavenumber  $K = 4$  and amplitude  $A = 0.06$  for Reynolds numbers of 600 and 1200 (given by Cases 8 and 9 in table 1). This increase in Reynolds number leads to a significant broadening of spectral dependence on the axial wavenumber within the cylinder wake, corresponding to a change whereby the streamwise vortices transform from the wider Mode A type to the narrower Mode B type (Williamson 1996). As the Reynolds number increases, we also observe more interaction between the vortex perturbations and the streamwise wake vortices.

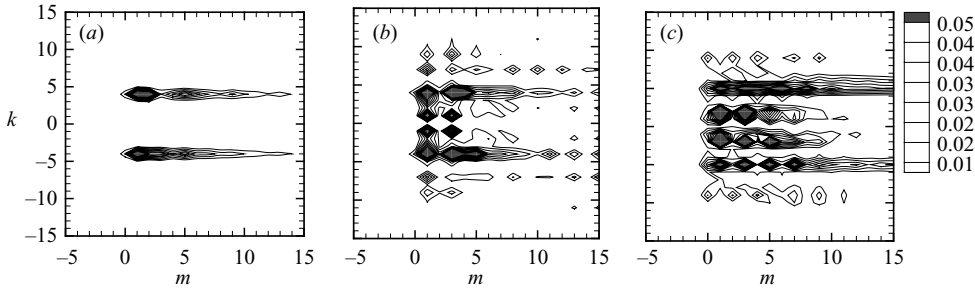


FIGURE 12. Contour plot showing first POD eigenvalue of the azimuthal vorticity component as a function of axial and azimuthal wavenumbers at time  $t=3$  for cases with (a)  $Re=300$  (Case 4), (b) 600 (Case 8), and (c) 1200 (Case 9).

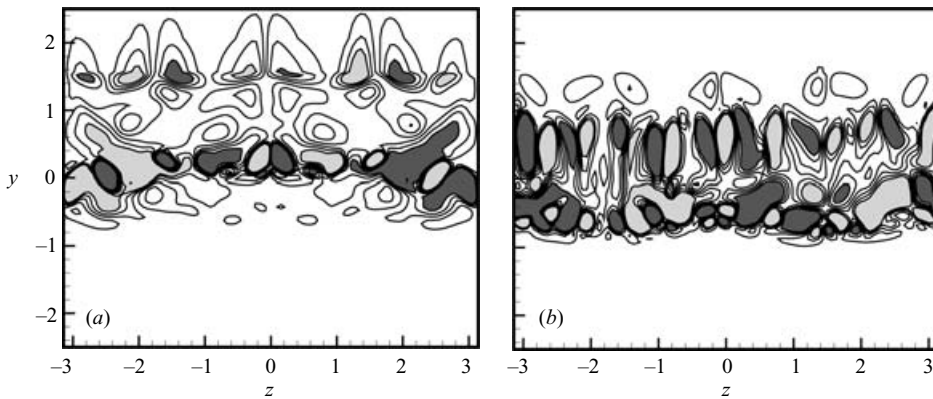


FIGURE 13. Streamwise vorticity ( $\omega_x$ ) contours at the cross-sectional plane  $x=1.4$  at time  $t=4$  for cases with (a)  $Re=600$  (Case 8) and (b)  $Re=1200$  (Case 9).

The effect of the spectral broadening at higher Reynolds numbers can be seen in figure 12, where we plot the first POD eigenvalue of the azimuthal vorticity component as a function of azimuthal and axial wavenumbers at time  $t=3$  for Reynolds numbers 300, 600, and 1200. For  $Re=300$  (figure 12a), the azimuthal vorticity is strongly dominated by the axial wavenumber mode ( $k=4$ ) of the initial helical perturbations, with azimuthal wavenumber dependence gradually decaying over the interval  $0 \leq m < 15$ . As Reynolds number increases to 600 and 1200 in figures 12(b) and 12(c), the flow exhibits broader variation with axial wavenumber throughout the interval  $|k| < 10$ . For  $Re=1200$ , the azimuthal wavenumber dependence also broadens, with the flow exhibiting strong POD eigenvalues even out to  $m=15$ .

The spectral broadening is also evident when examining the structure of the streamwise vortices within the cylinder wake. For instance, in figure 13 we plot the streamwise vorticity component ( $\omega_x$ ) on the cross-sectional plane  $x=1.4$  at time  $t=4$  for both the  $Re=600$  and 1200 cases. The corresponding plot for the case with  $Re=300$  is given in figure 7(d). In all of these figures, the bottom row of streamwise vorticity is due to the cylinder wake and the top row is a remnant of the impinging vortex structure. The transition from Mode A vortices to Mode B vortices within the cylinder wake is clearly evidenced by the shorter dominant length scale of the vortex structures along the bottom row in figures 13(a, b) compared to the  $k=2$  dominant structures in figure 7(d). In figure 13(a), the remnants of the incident vortex

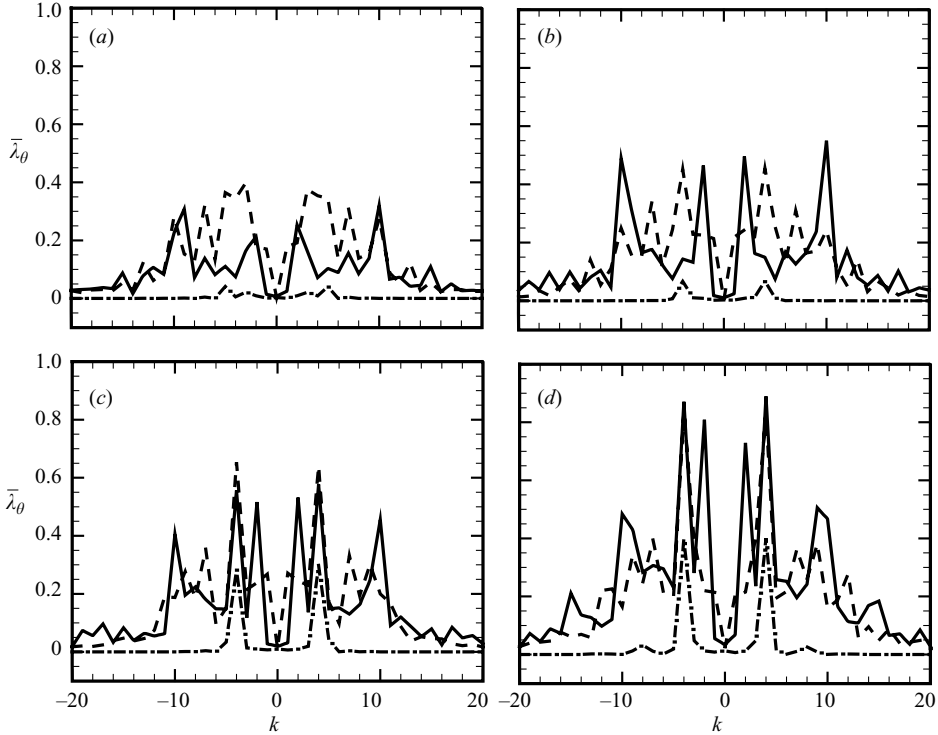


FIGURE 14. Plot of the first POD eigenvalue of the azimuthal vorticity component, summed over azimuthal wavenumbers, as a function of axial wavenumber at times (a)  $t = 1$ , (b) 2, (c) 3, and (d) 4 with Reynolds numbers  $Re = 300$  (Case 4; dashed-dotted line), 600 (Case 8; dashed line), and 1200 (Case 9; solid line).

perturbations for the  $Re = 600$  case appear to have maintained a  $k = 4$  dominance and to not significantly interact with the cylinder wake structures, as was also the case for  $Re = 300$ . By contrast, the vortex structures along the top row in figure 13(b) for the  $Re = 1200$  exhibit a much richer wavenumber spectrum and appear to be extending down and interacting with the wake vortex structures along the bottom row.

The first POD eigenvalue of the azimuthal vorticity component,  $\bar{\lambda}_\theta$ , is plotted in figure 14 as a function of axial wavenumber at four times for cases with Reynolds number 300, 600 and 1200. The  $Re = 300$  cases exhibits a narrow wavenumber dependence, confined primarily to  $k = 4$ , and generally has lower POD eigenvalues. The cases with  $Re = 600$  and 1200 have much broader wavenumber dependence in the interval  $-15 \leq k \leq 15$ , which, as discussed above, is due primarily to the richer wavenumber dependence within the cylinder wake at higher Reynolds numbers. Figure 14 indicates that even with this fuller wavenumber dependence, it is mainly the  $k = 4$  mode (matching the perturbation mode on the incident vortex) which amplifies significantly for the  $Re = 600$  case, indicating separation of the incident vortex amplification and the cylinder wake vortices. On the other hand, the  $Re = 1200$  case exhibits amplification in a number of wavenumber modes as the vortex approaches the cylinder, including very significant amplification for the  $k = 2$  and  $k = 10$  modes. It is not clear whether the broader wavenumber amplification at higher Reynolds numbers is due to interaction of the different perturbation modes of the impinging vortex with each other or to interaction of the impinging vortex with the cylinder



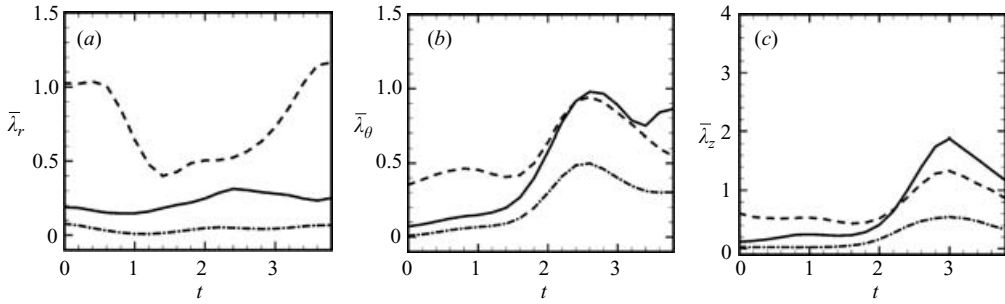


FIGURE 15. Time variation of the  $k=4$  mode of the POD eigenvalues (summed over the azimuthal wavenumbers) for the radial, azimuthal and axial vorticity components for cases with  $Re=300$  (Case 4; dashed-dotted line), 600 (Case 8; dashed line), and 1200 (Case 9; solid line).

wake, although figure 13(b) suggests that both processes may be occurring. The time variation of the  $k=4$  mode of the first POD eigenvalue of the three vorticity components  $\bar{\lambda}_r$ ,  $\bar{\lambda}_\theta$ , and  $\bar{\lambda}_z$  is plotted in figure 15 for  $Re=300$ , 600 and 1200. Both the azimuthal and axial vorticity components exhibit significant growth in time.

The amplification measures  $\bar{\lambda}_{z,H}$ ,  $\bar{\lambda}_{z,S}$ , and  $\bar{\lambda}_{z,I}$  for these higher Reynolds number cases ( $Re=600$  and 1200) are listed in table 2. Because of the broader spectral content of the cylinder wake at these Reynolds numbers, the ratio  $\bar{\lambda}_{z,H}/\bar{\lambda}_{z,S}$  is much smaller than it is for the  $Re=300$  case. Based on these measures, it appears that roughly two-thirds of the amplification measure  $\bar{\lambda}_{z,H}$  is due to amplification of the impinging vortex perturbations and about one-third is due to the streamwise vortices in the cylinder wake. The amplification ratio  $\bar{\lambda}_{z,H}/\bar{\lambda}_{z,I}$  is observed to increase with Reynolds number, having values of 19.3, 46.7, and 66.2 for cases with  $Re=300$ , 600 and 1200, respectively. Even if we reduce the values of this ratio by multiplying by a factor of  $2/3$  for the two higher Reynolds number cases to correct for the effect of the cylinder wake, the data still indicate that the amplification ratio increases substantially as the Reynolds number increases. This observation is consistent with the speculation from §2 that viscous diffusion between the impinging vortex and the cylinder boundary layer act to suppress amplification of the vortex perturbations.

## 6. Mode selection during three-dimensional wave amplification

A final computation was performed in order to examine the relative amplification rate for different vortex perturbation modes as the vortex impinges on the cylinder. In this computation (Case 10), the vortex is perturbed with equal-amplitude perturbations for all wavenumbers in the interval  $1 \leq k \leq 10$ , such that the vortex axis position at the initial time is given by

$$\mathbf{r}(z, t_0) = -c\mathbf{e}_x + \frac{A}{N} \sum_{n=1}^N [\cos(nz)\mathbf{e}_x - \sin(nz)\mathbf{e}_y], \quad (5)$$

where  $A=0.06$  and  $N=10$ . The initial perturbation amplitude for any one wavenumber is  $A/N=0.006$ .

The first POD eigenvalues of the radial, azimuthal, and axial vorticity components at time  $t=3$  are given as functions of the axial and azimuthal wavenumbers in figure 16. This figure indicates broad spectral variation in both axial and azimuthal

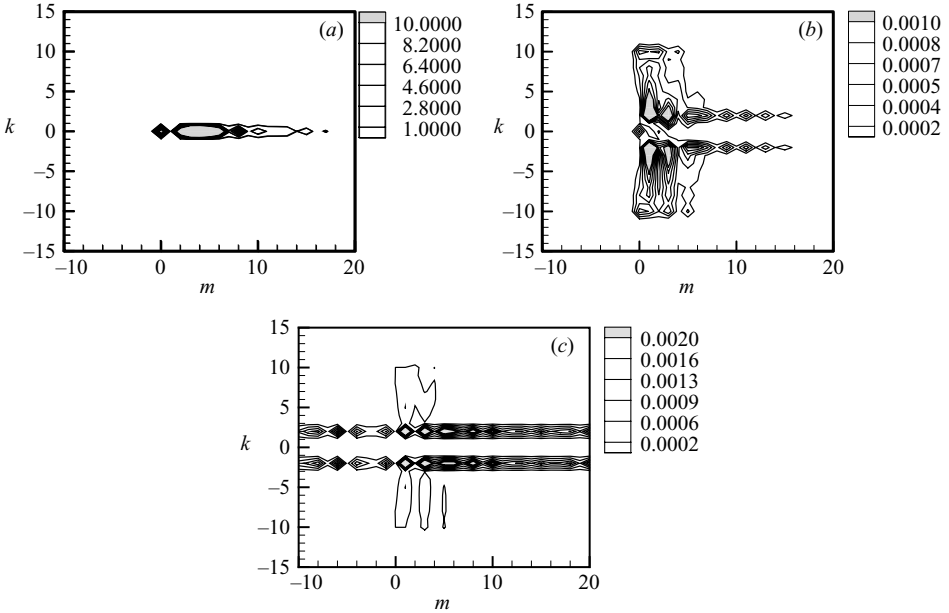


FIGURE 16. Contour plot showing first POD eigenvalue of the (a) radial, (b) azimuthal and (c) axial vorticity components as a function of axial and azimuthal wavenumbers at time  $t = 3$  for a case with initial perturbation given by equation (5) (Case 10).

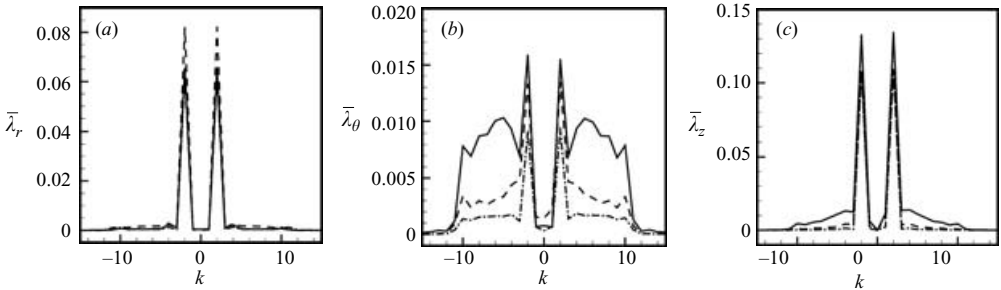


FIGURE 17. POD eigenvalues (summed over the azimuthal wavenumbers) for the (a) radial, (b) azimuthal and (c) axial vorticity components for a case with initial perturbation given by equation (5) (Case 10) at times  $t = 1$  (dashed-dotted line), 2 (dashed line), and 3 (solid line).

wavenumbers. The growth in time of the POD eigenvalues for all vorticity components is plotted as a function of axial wavenumber in figure 17, in which different curves are used to indicate the POD eigenvalues at time  $t = 1, 2, 3$  and 4 as the vortex structure approaches and impinges on the cylinder. Growth of the vortex perturbations is particularly apparent for the azimuthal vorticity component.

The amplification measures  $\bar{\lambda}_{z,H}$ ,  $\bar{\lambda}_{z,S}$ , and  $\bar{\lambda}_{z,I}$  are computed for each axial wavenumber in the interval  $1 \leq k \leq 10$ , and the results are listed in table 3. For wavenumbers  $k = 1$  and 2, the value of  $\bar{\lambda}_{z,S}$  is of the same order as the value of  $\bar{\lambda}_{z,H}$ , indicating that the cylinder wake makes a significant contribution to  $\bar{\lambda}_{z,H}$  for these wavenumbers. For  $k \geq 3$ , however,  $\bar{\lambda}_{z,S}$  is at least an order of magnitude smaller than  $\bar{\lambda}_{z,H}$ , so the ratio  $\bar{\lambda}_{z,H}/\bar{\lambda}_{z,I}$  should be an accurate measure of the vortex perturbation amplification for wavenumbers in this range. The maximum value of the amplification ratio in the

$k$	$\bar{\lambda}_{z,H}$	$\bar{\lambda}_{z,S}$	$\bar{\lambda}_{z,I}$	$\frac{\bar{\lambda}_{z,H}}{\bar{\lambda}_{z,I}}$	$\frac{\bar{\lambda}_{z,H}}{\bar{\lambda}_{z,S}}$
1	0.0120	0.0103	0.00147	8.16	1.17
2	0.137	0.124	0.000832	165	1.10
3	0.0134	$4.13 \times 10^{-5}$	0.000690	19.4	324
4	0.0139	0.00124	0.000525	26.5	11.2
5	0.0109	$5.05 \times 10^{-6}$	0.000448	24.3	2160
6	0.00847	$2.27 \times 10^{-5}$	0.000371	22.8	373
7	0.00592	$5.59 \times 10^{-7}$	0.000314	18.9	$1.06 \times 10^4$
8	0.00533	$6.27 \times 10^{-7}$	0.000306	17.4	$0.85 \times 10^4$
9	0.00348	$1.86 \times 10^{-7}$	0.000251	13.9	$1.87 \times 10^4$
10	0.00434	$1.06 \times 10^{-7}$	0.000409	10.6	$4.09 \times 10^4$

TABLE 3. Amplification measures as a function of axial wavenumber for Case 10.

interval  $k \geq 3$  is observed to occur for  $k = 4$ , with a gradual fall-off in amplification ratio as the wavenumber increases. The value of the amplification ratio for  $k = 4$  is found to be 26.5, which is very close to the value 26.4 obtained for Case 2 with the vortex initialized with only the  $K = 4$  perturbation (and initial wave amplitude  $A = 0.01$ ). Similarly, the amplification ratio for Case 10 with  $k = 8$  is found to be 17.4, which is reasonably close to the value 13.5 obtained for Case 7 with only the  $K = 8$  perturbation. The slightly lower amplification ratio for Case 7 may be due to the fact that the initial perturbation amplitude ( $A = 0.03$ ) for this case was somewhat higher than the effective amplitude  $A/N = 0.006$  for each wavenumber mode in Case 10. A similar slight reduction in amplification ratio with increase in perturbation amplitude is observed in comparing Cases 2–4. The observation that the amplification ratio has a similar value for Case 10, where a broad spectrum of perturbations is present, and in cases where only one wavenumber perturbation is present suggests that, at least for small perturbation amplitude, there is not significant interaction between perturbation modes with different axial wavenumbers.

It is of interest to compare the wavelength associated with the observed fastest-growing  $k = 4$  perturbation ( $L = 2\pi/k \approx 1.6$ ) with other length scales associated with the problem. For instance, this fastest-growing wavelength is reasonably close to the cylinder diameter, which has a length  $d = 1$ . As noted in §1 of the paper, the perturbation amplification is hypothesized to be associated with instability of the vortex under the straining flow near the front stagnation point of the cylinder flow field. For the problem of a vortex with elliptical cross-section in a plain straining flow, Landman & Saffman (1987) report that instability occurs only for wavenumbers where the Ekman number, define by  $E_\nu = 2\pi\nu k^2/\gamma$ , lies in the interval  $0 \leq E_\nu \leq 1$ . Here  $\nu$  is the kinematic viscosity,  $k$  is the vortex axial wavenumber, and  $\gamma$  is half of the vorticity within the ambient vortex core. For the case considered in this section, this result indicates that the straining instability will occur within the interval  $0 < k < 17.4$ . The most unstable axial wavenumber for a vortex with nearly circular cross-section in a straining flow was examined by Moore & Saffman (1975) and Tsai & Widnall (1976). These investigators find, using several different methods, that the most unstable bending wave on the vortex occurs for an axial wavenumber of  $k\sigma = 2.5$ . For the core radius value  $\sigma = 0.5$  used in this section, we obtain the most unstable wavenumber as  $k = 5$ , corresponding to a wavelength of  $L = 2\pi/k \approx 1.3$ . The fact that both the cylinder diameter and the most-unstable vortex straining instability

wavelength are relatively close to the observed wavelength of the fastest-growing wave in our calculations makes it difficult to clearly associate the observed wave amplification with a specific one of these scalings.

## 7. Conclusions

Parallel vortex–cylinder interaction is examined for three-dimensional viscous flows, focusing on the amplification of three-dimensional perturbations as a vortex impinges on a cylinder. The growth of these perturbations is quantified using a proper orthogonal decomposition (POD) approach based on the Fourier-transformation of the vorticity vector in the axial and azimuthal directions and a POD eigenvector fit in the radial direction. This approach yields clear information on the time variation of the enstrophy associated with different components of the vorticity field as functions of the axial and azimuthal wavenumbers. Summation of the POD eigenvalues over the azimuthal wavenumbers yields a measure of the growth of the vortex perturbations as a function of axial wavenumber alone. To further quantify the growth of three-dimensional perturbations, a set of three amplification measures is defined that provides an indication of the peak value of the perturbation enstrophy as the vortex impinges on the cylinder, of the initial value of the perturbation enstrophy, and of the peak enstrophy due to the cylinder wake, all of which are evaluated at the axial wavenumber associated with the imposed vortex perturbation. Ratios of these measures are used to deduce the degree to which the cylinder wake contributes to the POD eigenvalues at that wavenumber and the degree of amplification of the vortex perturbation as the vortex approaches the cylinder.

Cases with different values of the initial helical perturbation amplitude  $A = a/d$  and wavenumber  $K = k_p d$  are examined for three different Reynolds numbers. Significant amplification of three-dimensional vortex perturbations is observed for all cases. For low Reynolds number cases ( $Re = 300$ ), the amplification is confined mainly to the prescribed wavenumber of the initial vortex perturbation, and the evolution of the vortex perturbation is not significantly influenced by the streamwise vortex structures within the cylinder wake. The amplification ratio is observed to be nearly independent of the incident vortex initial perturbation amplitude for small values of the initial amplitude, but to depend on perturbation initial wavenumber and the flow Reynolds number. Maximum amplification is observed for initial perturbation axial wavenumber of approximately  $K = 4$ , corresponding to a wavelength approximately equal to 1.5 times the cylinder diameter. As the Reynolds number is increased (up to  $Re = 1200$ ), a broader spectrum of axial wavenumber modes is observed in both the cylinder wake and the vortex amplification response. The amplification ratio increases significantly with increase in Reynolds number, which supports the speculation that viscous diffusion between the vortex and the cylinder boundary layer suppresses amplification of the vortex three-dimensional perturbations.

In order to examine competition between different axial wavenumber modes, a computation is performed where a spectrum of different initial perturbations is introduced on the vortex, with axial wavenumbers spanning from 1 to 10. The  $k = 4$  wavenumber mode is again observed to have the largest amplification ratio, with gradual decrease in amplification ratio as the wavenumber increases. The different perturbation modes have little interaction for cases with small initial perturbation amplitude, such that the amplification ratio observed for a computation with a broad spectrum of axial wavenumbers present is close to that observed with only one axial wavenumber in the initial vortex perturbation.

The present paper shows that even in cases where the incident vortex appears to be aligned in such a manner that the vortex-body interaction is nearly two-dimensional, small three-dimensional perturbations on the impinging vortex grow significantly as the vortex impacts upon the cylinder face. Even for the relatively low Reynolds number cases examined in this paper, the enstrophy associated with the three-dimensional vortex perturbations is observed to increase to well over an order of magnitude greater than its initial value as the vortex impacts upon the cylinder. Increase in Reynolds number only serves to increase the amplification ratio. These three-dimensional perturbations lead to the formation of streamwise vortex structures which are eventually swept into the cylinder wake, to join the streamwise cylinder wake vortices that naturally occur in Kármán vortex street wakes.

The above discussion indicates that parallel vortex-body interaction is not a strictly two-dimensional flow problem, even for cases where the mean flow appears to be two-dimensional. This is, of course, also the case even for the simpler problem of uniform flow past a cylinder, where the two-dimensional flow structure breaks down with the formation of streamwise wake vortices at about  $Re = 190$ . On the other hand, the three-dimensional vortex perturbations are found to have remarkably little effect on the cylinder force variation during vortex impact, even for cases with initial vortex wave perturbation amplitudes of up to 20 % of the vortex diameter.

This project was supported by the US Office of Naval Research under grant number N00014-01-1-0015. Dr Thomas Swain is the program manager.

#### REFERENCES

- BARKLEY, D. & HENDERSON, R. D. 1996 Three-dimensional Floquet stability analysis of the wake of a circular cylinder. *J. Fluid Mech.* **322**, 215–241.
- BRIKA, D. & LANEVILLE, A. 1997 Wake interference between two circular cylinders. *J. Wind Engng Ind. Aerodyn.* **72**, 61–70.
- BRITTER, R. E., HUNT, J. C. R. & MUMFORD, J. C. 1979 The distortion of turbulence by a circular cylinder. *J. Fluid Mech.* **92**, 269–301.
- FLEISCHMANN, S. T. & SALLET, D. W. 1981 Vortex shedding from cylinders and the resulting unsteady forces and flow phenomenon. Part I. *Shock Vib. Digest* **13**(10), 9–22.
- GAMARD, S., GEORGE, W. K., JUNG, D. & WOODWARD, S. 2002 Application of a ‘slice’ proper orthogonal decomposition to the far field of an axisymmetric turbulent jet. *Phys. Fluids* **14**, 2515–2522.
- HOLMES, P., LUMLEY, J. L. & BERKOOZ, G. 1996 *Turbulence, Coherent Structures, Dynamical Systems and Symmetry*. Cambridge University Press.
- HUNT, J. C. R. 1973 A theory of turbulent flow round two-dimensional bluff bodies. *J. Fluid Mech.* **61**, 625–706.
- ISSA, R. 1985 Solution of the implicit discretized fluid flow equations by operator splitting. *J. Comput. Phys.* **62**, 40–65.
- KIYA, M., ARIE, M., TAMURA, H. & MORI, H. 1980 Vortex shedding from two circular cylinders in staggered arrangement. *Trans. ASME: J. Fluids Engng* **102**, 166–173.
- LAI, Y. G. 2000 Unstructured grid arbitrarily shaped element method for fluid flow simulation. *AIAA J.* **38**, 2246–2252.
- LANDMAN, M. J. & SAFFMAN, P. G. 1987 The three-dimensional instability of strained vortices in a viscous fluid. *Phys. Fluids* **30**, 2339–2342.
- LI, J., CHAMBAREL, A., DONNEAUD, M. & MARTIN, R. 1991 Numerical study of laminar flow past one and two circular cylinders. *Computers Fluids* **19**(2), 155–170.
- MITTAL, S., KUMAR, V. & RAGHUVANSHI, A. 1997 Unsteady incompressible flows past two cylinders in tandem and staggered arrangements. *Intl J. Numer. Meth. Fluids* **25**, 1315–1344.
- MOORE, D. W. & SAFFMAN, P. G. 1975 The instability of a straight vortex filament in a strain field. *Proc. R. Soc. Lond. A* **346**, 413–425.

- RAMBERG, S. 1983 The effects of yaw and finite length upon the vortex wakes of stationary and vibrating circular cylinders. *J. Fluid Mech.* **128**, 81–107.
- ROCKWELL, D. 1998 Vortex-body interactions. *Ann. Rev. Fluid Mech.* **30**, 199–229.
- SUN, J., LI, J. & ROUX, B. 1993 Flow regimes and frequency selection of a cylinder oscillating in an upstream cylinder wake. *Intl J. Numer. Meth. Fluids* **16**, 915–929.
- THAKUR, A., LIU, X. & MARSHALL, J. S. 2004 Wake flow of single and multiple yawed cylinders. *Trans. ASME: J. Fluids Engng* **126**, 861–870.
- TSAI, C. Y. & WIDNALL, S. E. 1976 The stability of short waves on a straight vortex filament in a weak externally imposed strain field. *J. Fluid Mech.* **73**, 721–733.
- WILLIAMSON, C. H. K. 1996 Vortex dynamics in the cylinder wake. *Ann. Rev. Fluid Mech.* **28**, 477–539.
- ZDRAVKOVICH, M. M. 1977 Review of flow interference between two circular cylinders in various arrangements. *Trans. ASME: J. Fluids Engng* **99**, 618–633.